Supplementary Information

An integrated hydrodeoxygenation-hydroisomerization strategy for biofuel production from cashew nut shell liquid

Dekang Kong,[a] Xuan Guo,[b] Pei Hu,[a] Yudi Zhao,[a] Junhao Wang,[a] Huili Zhang,*[c] Yunming Fang*[a]

a. State Key Laboratory of Green Biomanufacturing, Beijing University of Chemical Technology, Beijing 100029, P.R. China. E-mail: fangym@mail.buct.edu.cn

b. Yantai Vocational College, Yantai 264670, P.R. China

c. School of Life Science and Technology, Beijing University of Chemical Technology, Beijing 100029, P.R. China

Contents

Supplementary Note 1 Methodology for Mass and Carbon Balance Analysis, Productivity and space-time yield Calculation：

The over mass balance closure was calculated according to:

$$Mass\ balance\ closure(\%) = \frac{m_{org} + m_{aq} + m_{gas} + m_{coke}}{m_{feed} + m_{H_2,in}} \times 100\%\#(1)\#$$

Where m_{feed} and $m_{H_2,in}$ represent the masses of feedstock and hydrogen introduced into the reactor during the defined steady-state collection interval; m_{org}, m_{aq}, m_{gas} and m_{coke} represent the masses of the organic liquid phase, aqueous phase, gaseous products and deposited coke collected or assigned within the same interval.

The carbon balance closure was calculated according to:

$$Carbon\ balance\ closure(\%) = \frac{m_{C,org} + m_{C,aq} + m_{C,gas} + m_{C,coke}}{m_{C,feed}} \times 100\%\#(2)\#$$

$$m_{C,feed} = m_{feed} * C_{feed}\#(3)$$

$$m_{C,org} = m_{org} * C_{org}\#(4)\#$$

Where $m_{C,feed}$ is the mass of carbon introduced with the feedstock; $m_{C,org}$, $m_{C,aq}$, $m_{C,gas}$ and $m_{C,coke}$ are the masses of carbon distributed in the organic liquid, aqueous, gas, and coke phases. Here, C_{feed} and C_{org} are the carbon mass fraction of the feedstock and the organic liquid product, as determined by elemental analysis during the steady-state collection interval.

For the balance analysis, the steady-state interval after 10 h on stream was selected. Under these conditions, coke formation was considered to be much lower than that in the initial reaction stage, where catalyst activity was higher and side reactions were more severe. Because direct quantification of coke formed specifically within the defined steady-state collection interval was not feasible, the contribution of coke during this period was considered negligible for the balance calculation, and thus m_{coke} and $m_{C,coke}$ were approximated as 0.

In addition, no obvious organic products were observed in the aqueous phase collected during the same steady-state interval. Therefore, the carbon contribution of the aqueous phase was considered negligible compared with those of the organic liquid and gas phases, and $m_{C,aq}$ was approximated as 0 in the carbon balance calculation.

Importantly, gaseous products were explicitly quantified and included in both calculations. The gas volume was measured using a wet gas meter, and the gas composition was determined by micro-GC. Therefore, the gas phase was quantitatively considered rather than neglected in the balance analysis.

To quantitatively describe the catalytic performance of the integrated continuous fixed-bed system, we report productivity and space-time yield (STY) using two product definitions.[1,2] The first is based on

the hydrocarbon products in the organic phase, for which:

$$Productivity_{org} = \frac{m_{org}}{m_{cat,total} \times t}$$

$$STY_{org} = \frac{m_{org}}{V_{bed,total} \times t}$$

The second is based on the fuel-relevant product fraction, defined here as C7-C20 hydrocarbons together with the isomerized products (IP) fraction, for which:

$$Productivity_{fuel} = \frac{m_{C7-C20+IP}}{m_{cat,total} \times t}$$

$$STY_{fuel} = \frac{m_{C7-C20+IP}}{V_{bed,total} \times t}$$

where m_{org} is the mass of the organic phase, $m_{C7-C20+IP}$ is the mass of the C7-C20 hydrocarbons and IP products collected during the defined steady-state interval, t is the collection time, $m_{cat,total}$ is the total mass of the catalysts loaded in the HDO and hydroisomerization beds, and $V_{bed,total}$ is the total packed catalyst-bed volume of the HDO and hydroisomerization catalyst layers, excluding inert Al_2O_3 ceramic beads and other non-catalytic packing materials. These definitions have now been explicitly added in the revised manuscript to avoid ambiguity in the dual-bed system.

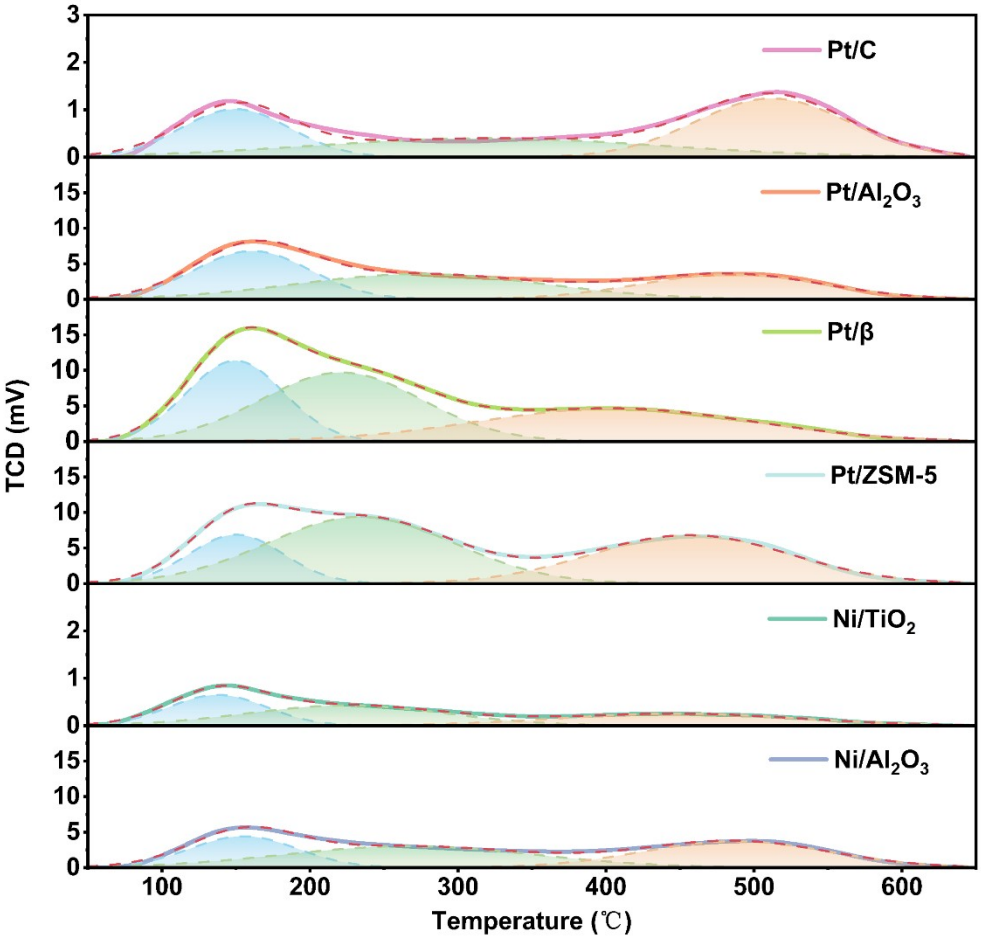

Fig. S1 NH_3-TPD profiles of different HDO catalysts

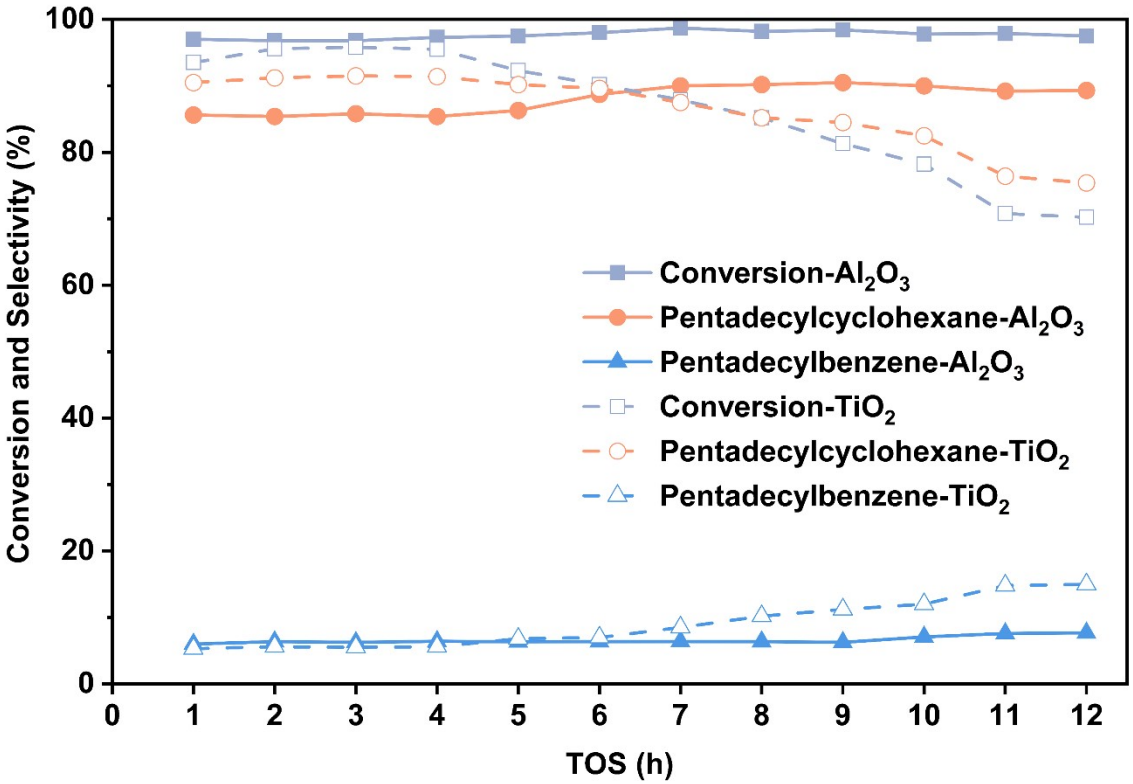

Fig. S2 Stability of Ni/Al_2O_3 and Ni/TiO_2 catalysts

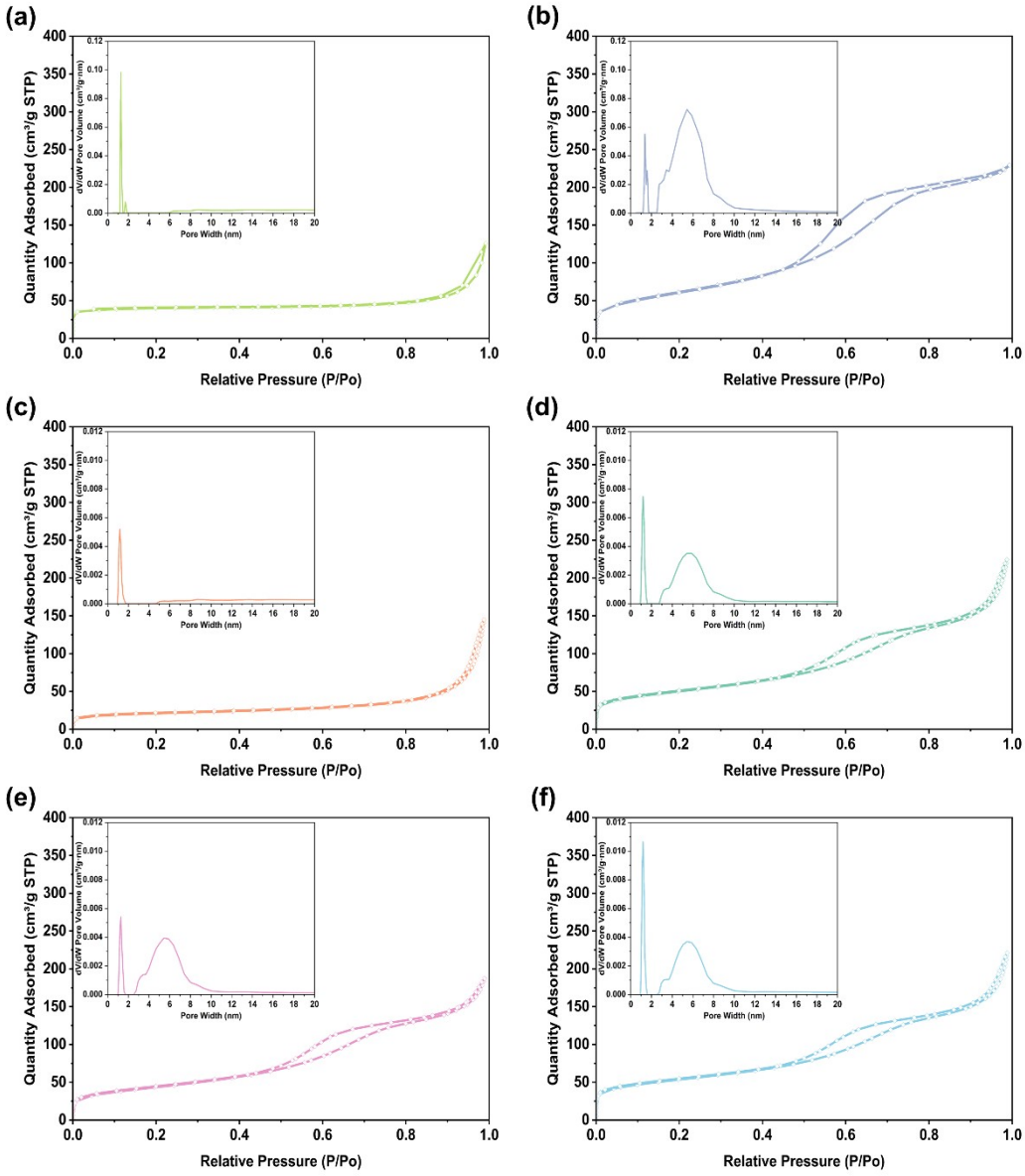

Fig. S3 N_2 physisorption isotherms of different Pt-based bifunctional catalysts, with the BJH pore size distribution derived from the adsorption branch as insert (a) ZSM-22 (b) Al_2O_3 (c) Pt/ZSM-22 (d) Pt-A/Z (e) Pt-Z/A (f) Pt/A+Z. Pt/A+Z referring to Pt/A+Z(Powder).

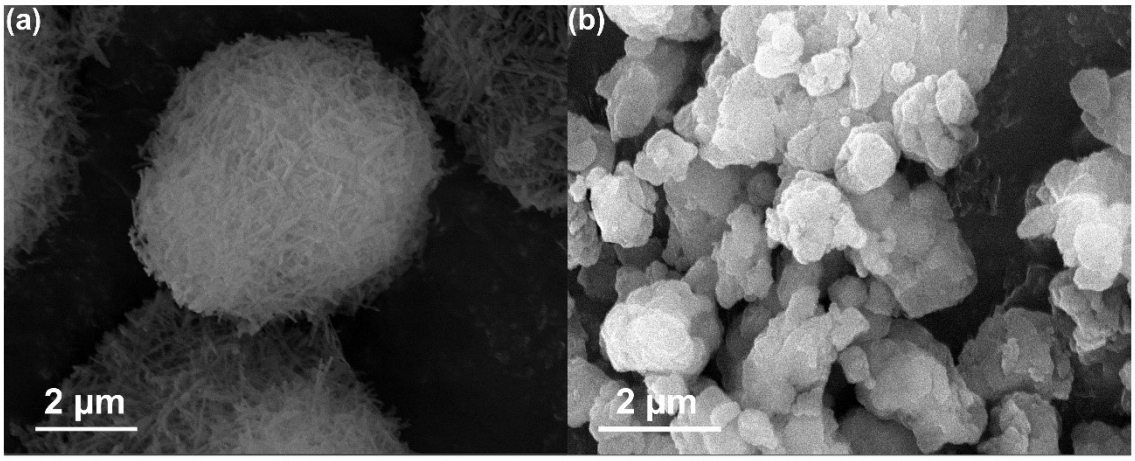

Fig. S4 SEM images of parent (a) ZSM-22 and (b) Al_2O_3

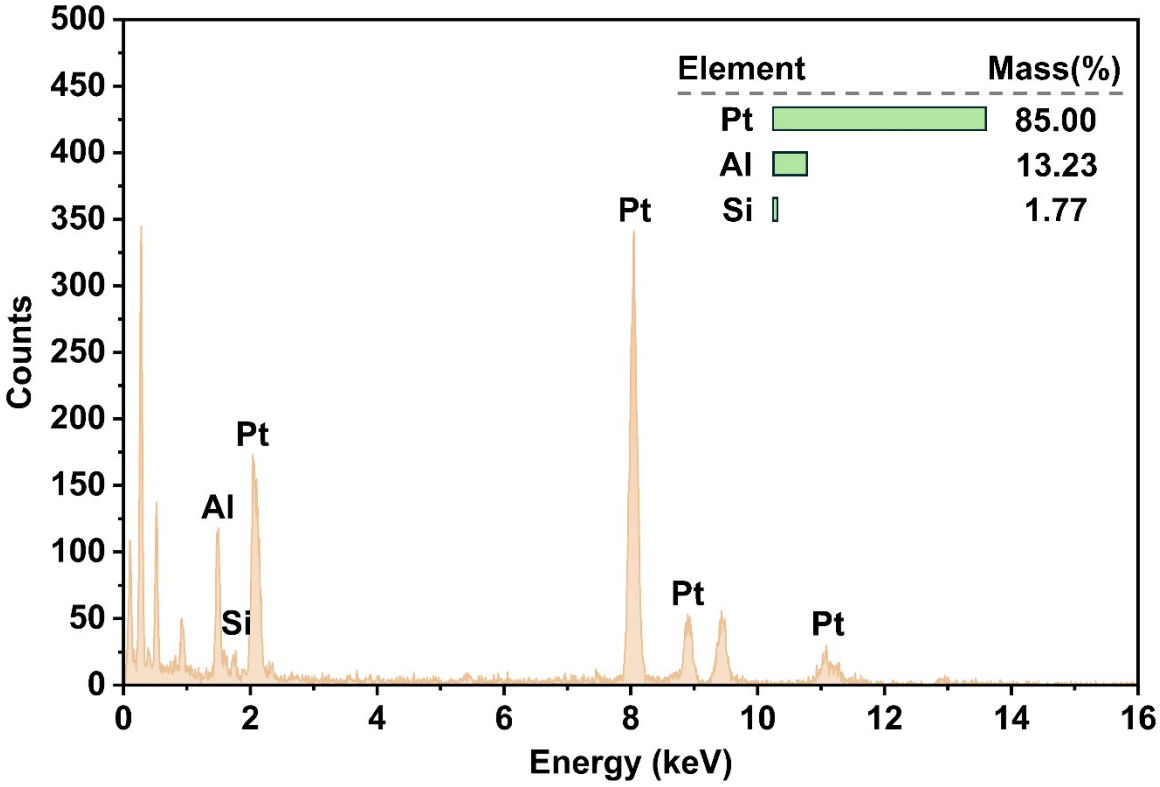

Fig. S5 Quantitative elemental analysis derived from the EDS spectrum acquired at Spot 1

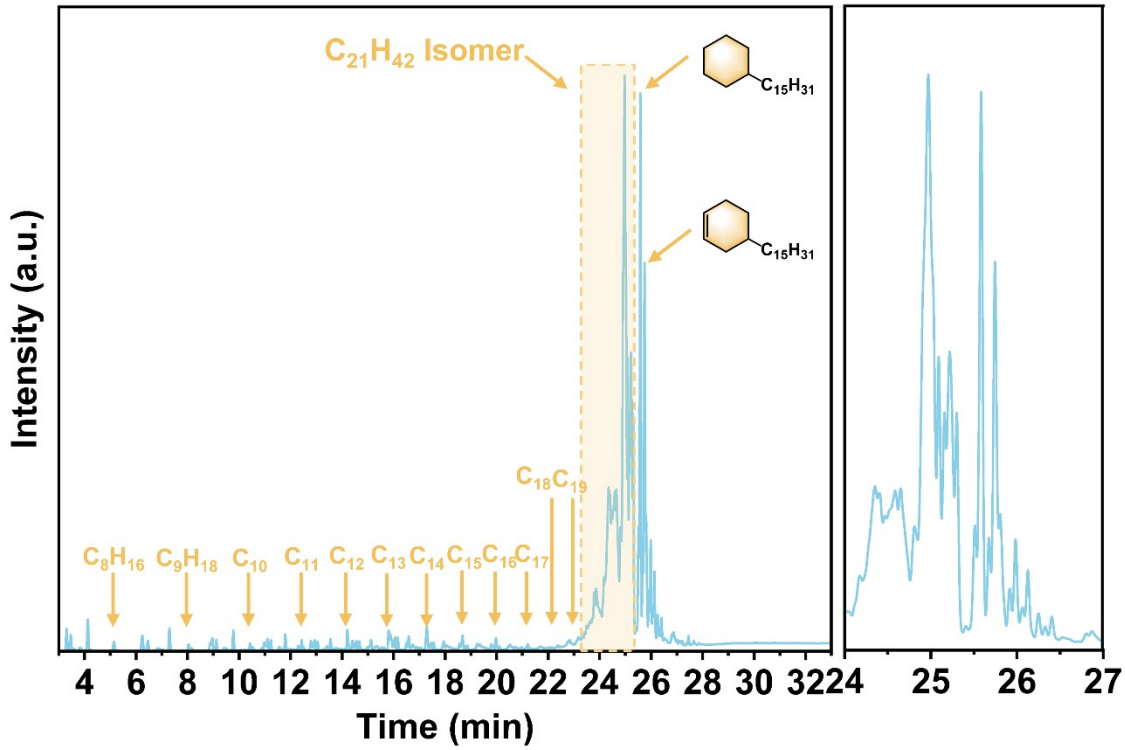

Fig. S6 Gas chromatogram of the liquid obtained after 5 h of reaction over the Pt-A/Z catalyst. Reaction conditions: CNSL flow rate, 0.1 mL min^{-1}; H_2/CNSL, 2000; pressure, 4 MPa; temperature, 350 °C; HDO catalyst Ni/Al_2O_3; $WHSV_1$, 1.67 h^{-1}; $WHSV_2$, 0.83 h^{-1}

Supplementary Note 2 Assignment and quantification of liquid-phase products by GC analysis

Figure S6 shows the gas chromatogram of the liquid obtained after 5 hours of reaction over the Pt-A/Z catalyst. In the figure, the C8 peak corresponds to ethylcyclohexane (as determined based on standard solution calibration), while the C9 and C10 peaks correspond to their respective linear alkylcyclohexanes. To calculate the concentration of C10, the chromatographic peak area between C9 and the C10 peak is assigned to the C10 component, and quantification is performed based on the standard curve for C10 cycloalkanes. The same method is applied to calculate the components for other carbon numbers (C7–C20), and their total mass is used to determine the mass yield of C7–C20 products. The orange-shaded region in the figure corresponds to peaks that, in GC-MS analysis, all showed a relative molecular mass of 294, with no other substances detected. Therefore, this segment of chromatographic peaks is uniformly labeled as C21 isomeric components. All components eluting after pentadecylcyclohexane are defined as heavy products.

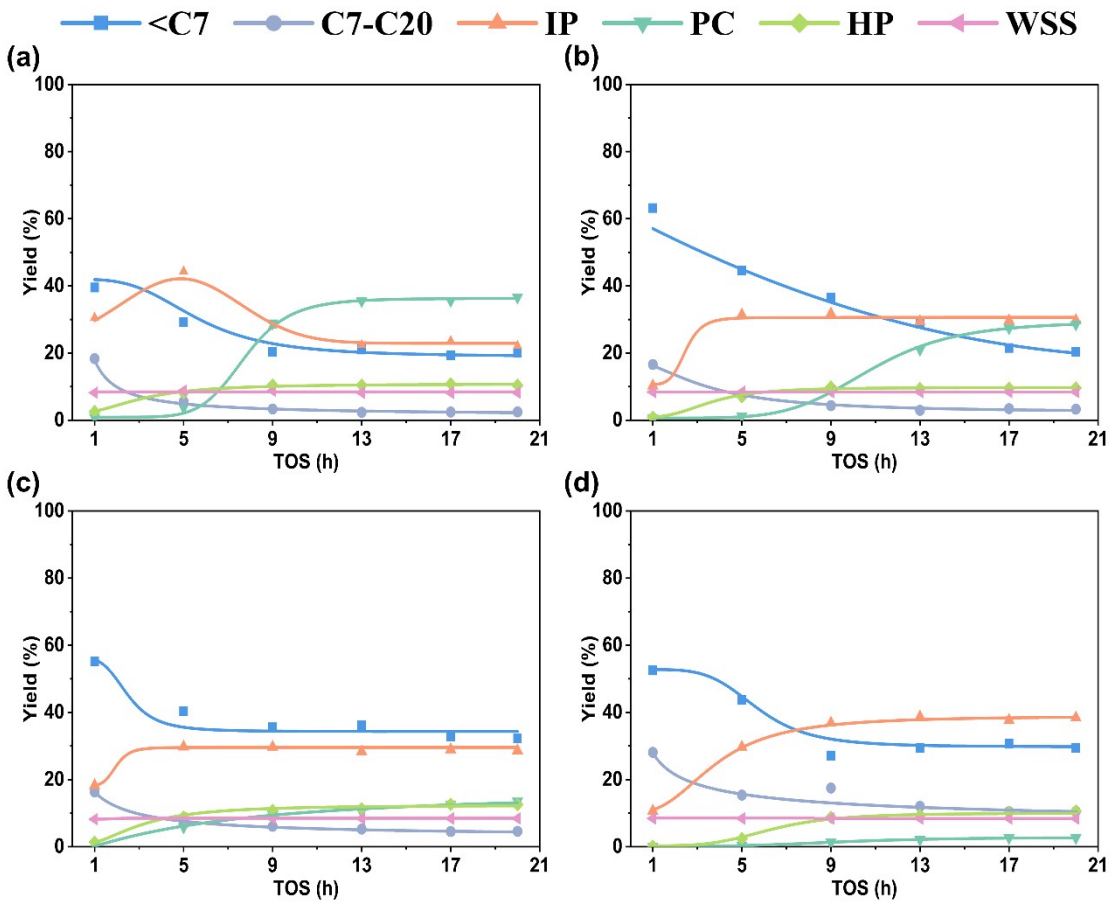

Fig. S7 Product distribution after the reaction of Pt-A/Z catalyst at different temperatures: (a) 350℃ (b) 360 ℃ (c) 370 ℃ (d) 380 ℃. Reaction conditions: CNSL flow rate,0.1 mL/min; H_2/CNSL, 2000; pressure, 4 MPa; HDO catalyst, Ni/Al_2O_3; Hydroisomerization catalyst, Pt-A/Z; $WHSV_1$, 1.67 h^{-1}; $WHSV_2$, 0.83 h^{-1}

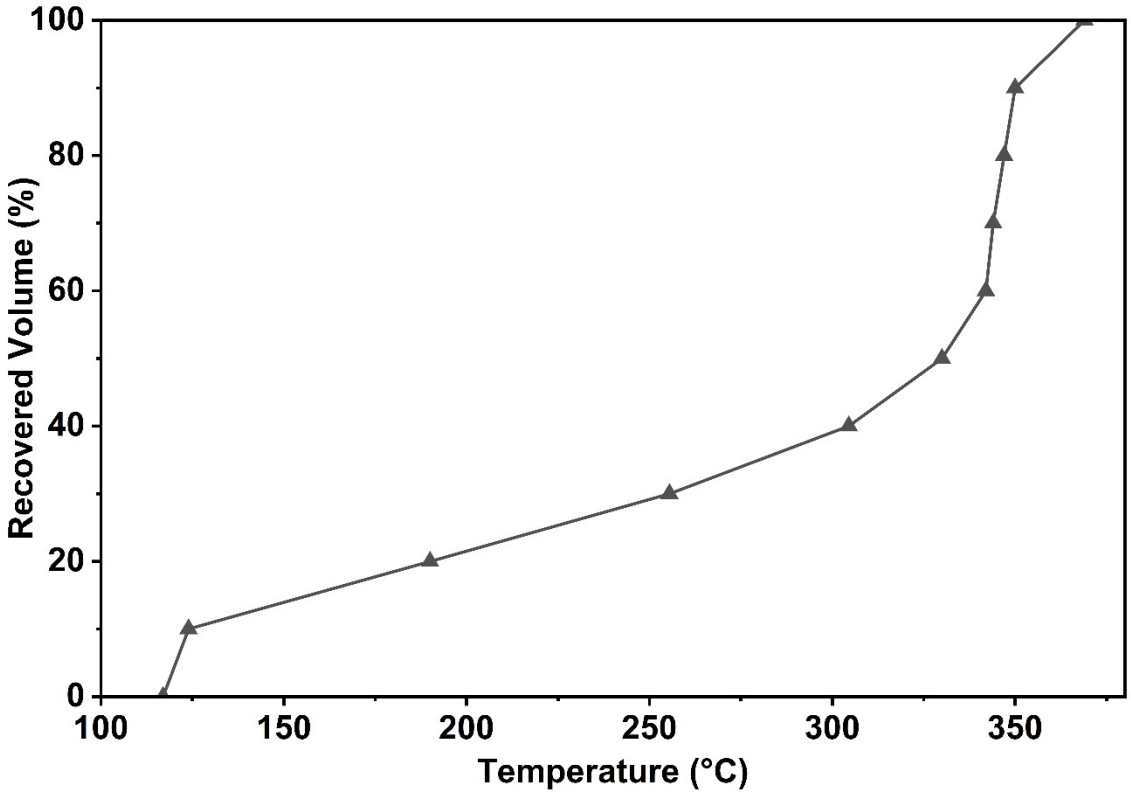

Fig. S8 Distillation curve of the mixed liquid product collected during the stable reaction period (11-20 h). Reaction conditions: CNSL flow rate, 0.1 mL min^{-1}; H_2/CNSL, 2000; pressure, 4 MPa; temperature, 360 ℃; HDO catalyst, Ni/Al_2O_3; Hydroisomerization catalyst, Pt-A/Z; $WHSV_1$ 0.53 h^{-1}; $WHSV_2$ 0.83 h^{-1}.

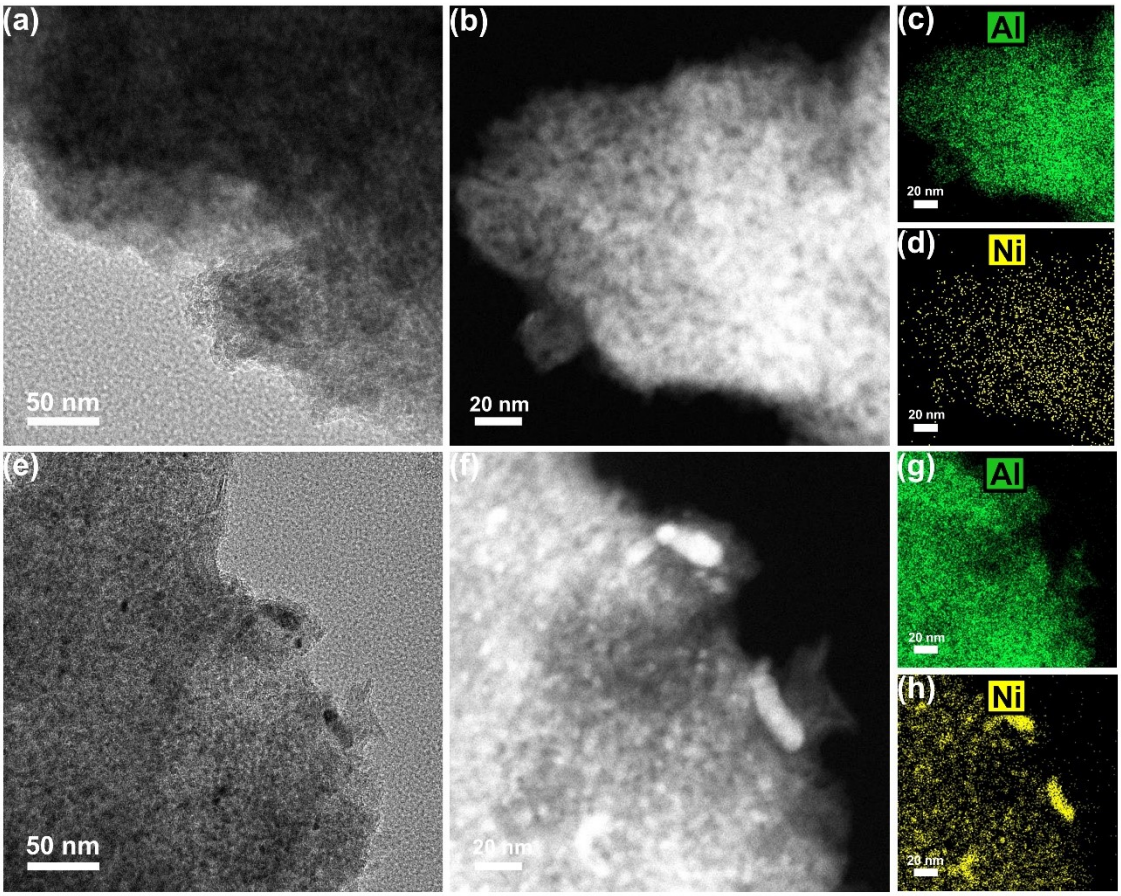

Fig. S9 TEM images of fresh and spent Ni/Al_2O_3, where (a) and (e) show the overall morphology of the fresh and spent samples. HAADF-STEM images of (b) fresh Ni/Al_2O_3 and (f) spent Ni/Al_2O_3 are presented. The corresponding EDS elemental mappings of the fresh catalyst (c-d) and spent catalyst (g-h) display the individual spatial distribution of Al and Ni.

Supplementary Note 3 TEM/HAADF-STEM and EDS analysis of fresh and spent Ni/Al_2O_3

The TEM/HAADF-STEM and EDS elemental mapping results (Fig. S9) indicate that the Ni/Al_2O_3 catalyst underwent a certain degree of structural evolution during the reaction. For the fresh catalyst, because the Ni species and the Al_2O_3 support exhibit similar contrast in conventional TEM images, it is difficult to directly distinguish the distribution of Ni species by bright-field TEM alone.[3] However, HAADF-STEM imaging and Ni elemental mapping clearly show that the Ni species are highly dispersed on the surface of the Al_2O_3 support, with no obvious large-scale Ni-enriched regions observed. In contrast, in the spent catalyst, locally brighter regions appeared, and the Ni elemental distribution changed from a relatively uniform dispersed state to a locally enriched one, indicating partial aggregation of the Ni species during the reaction. It should be noted that this aggregation mainly manifests as local nanoscale enrichment, without forming large continuous agglomerates, suggesting that although Ni sintering occurred, its extent is limited.

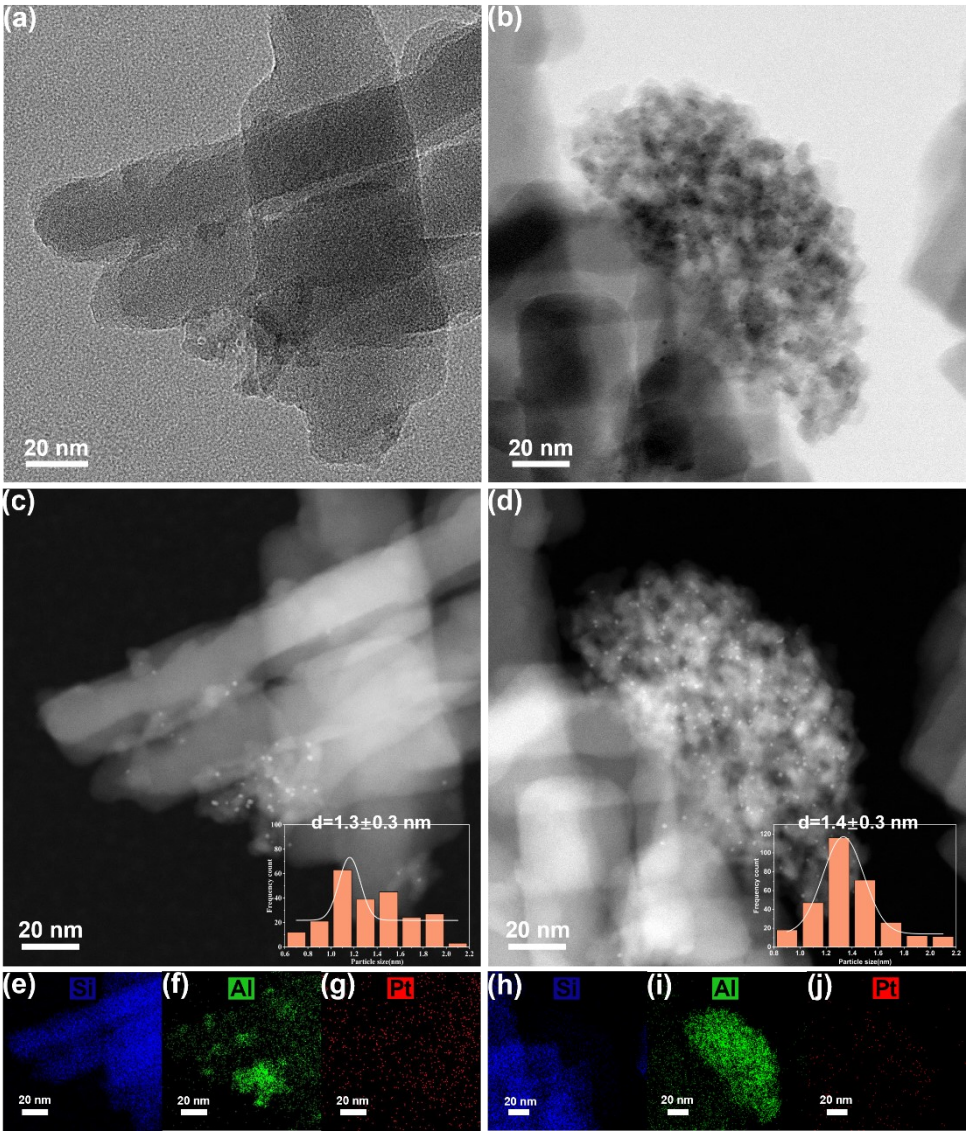

Fig. S10 TEM images of the fresh and spent Pt-A/Z catalyst, where (a) and (b) show the overall morphology of the fresh and spent samples. HAADF-STEM images of (c) fresh Pt-A/Z and (d) spent Pt-A/Z are presented, with the insets showing the corresponding particle size distribution of Pt nanoparticles. The corresponding EDS elemental mappings of the fresh catalyst (e-g) and spent catalyst (h-j) display the individual spatial distribution of Si, Al and Pt.

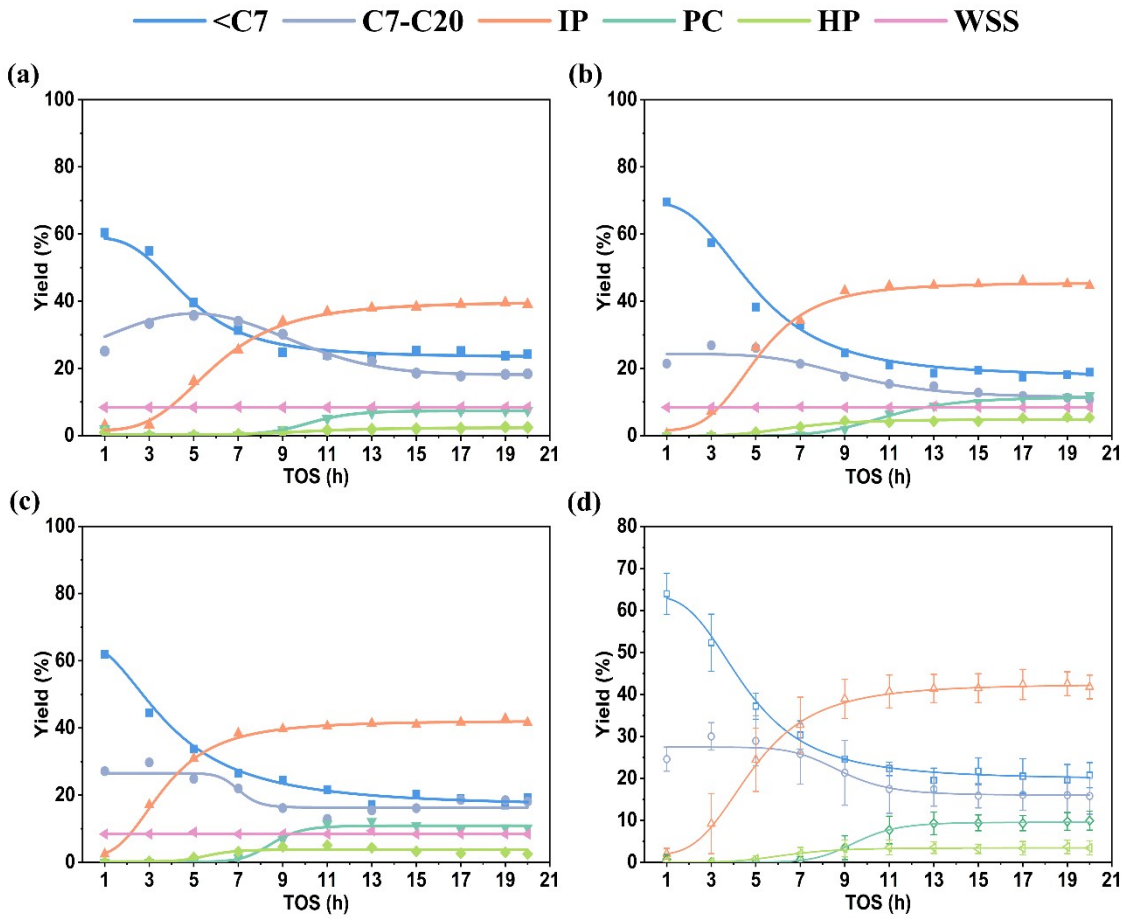

Fig. S11 Time-on-stream product distributions obtained from three independent replicate experiments under the optimal conditions. (a-c) Individual replicate runs and (d) mean values with error bars from three experiments. Reaction conditions: CNSL flow rate, 0.1 mL min^{-1}; H_2/CNSL, 2000; pressure, 4 Mpa; temperature, 360 °C; HDO catalyst, Ni/Al_2O_3; Hydroisomerization catalyst, Pt-A/Z; $WHSV_1$ 0.55 h^{-1}. $WHSV_2$ 0.83 h^{-1}.

Supplementary Note 4 Reproducibility and statistical analysis of product distribution

The time-dependent product distributions obtained from three independent replicate experiments (Fig. S11) demonstrated that the tandem hydrodeoxygenation-hydroisomerization system exhibited good reproducibility under the optimal reaction conditions. Although some fluctuations were observed during the initial stage of the reaction (approximately 1–7 h) across the three runs, the overall trends were highly consistent: the yield of <C7 light products gradually decreased over time, the yield of isomerized products increased rapidly before stabilizing, and the yields of pentadecylcyclohexane and heavy products gradually reached steady levels in the later stage. The mean values and error bars further indicate that the initial stage showed relatively large variability, whereas after approximately 9 h, the distribution of major products stabilized, and the error bars narrowed significantly. This suggests that the system underwent an initial transient period before reaching a stable operating state during the initial continuous operation period, after which the catalytic behaviour exhibited good reproducibility and operational robustness.

Table S1 Properties of CNSL

Property	Details
Composition (wt.%)[a]	Cardanol:93.78 Cardol:2.12 2-Methyl Cardol:1.64 Anacardic Acid:0.72
Elemental Analysis (wt.%)[b]	C:81.07 H:12.16 O:6.64
Density (kg m^{-3})[c]	20 ℃ 972 40 ℃ 959
Viscosity (mm^2 s^{-1})[d]	20 ℃ 75.3 40 ℃ 27.6

[a] By Gas Chromatography

[b] By CHONS Elemental Analyzer

[c] ASTM D4052

[d] ASTM D445.

Table S2 The textural properties of HDO catalysts from nitrogen physisorption experiments

Catalysts	S_{BET} (m^2 g^{-1})	S_{micro} (m^2 g^{-1})[a]	S_{ext} (m^2 g^{-1})[a]	V_{total} (cm^3 g^{-1})[b]	V_{micro} (cm^3 g^{-1})[a]	V_{meso} (cm^3 g^{-1})[c]
Ni/TiO_2	10.0	-	-	0.10	-	-
Ni/Nb_2O_5	1.3	-	-	0.02	-	-
Ni/Al_2O_3	179.4	48.8	130.6	0.33	0.02	0.31
Pt/Al_2O_3	187.9	50.1	137.8	0.35	0.02	0.33
Pt/C	677.9	507.3	170.6	0.37	0.24	0.13
Pt/ZSM-5	333.6	240.8	92.8	0.20	0.11	0.09
Pt/β	478.8	382.4	96.4	0.39	0.18	0.21

[a] t-plot method

[b] less than 167.7 nm diameter at P/P_0=0.988

[c] $V_{meso}=V_{total}-V_{micro}$

Table S3 The textural properties of samples from nitrogen physisorption experiments

Samples	Si/Al atomic ratio[a]	S_{BET} ($m^2\ g^{-1}$)	S_{micro} ($m^2\ g^{-1}$)[b]	S_{ext} ($m^2\ g^{-1}$)[b]	V_{total} ($cm^3\ g^{-1}$)[c]	V_{micro} ($cm^3\ g^{-1}$)[b]	V_{meso} ($cm\cdot g^{-1}$)[d]
ZSM-22	34	155	132	23	0.19	0.05	0.14
Al_2O_3	——	222	24	198	0.35	0.03	0.32
Pt/ZSM-22	——	76	39	37	0.22	0.01	0.21
Pt-A/Z	——	177	59	118	0.35	0.02	0.34
Pt-Z/A	——	156	45	111	0.29	0.01	0.28
Pt/A+Z	——	187	72	115	0.34	0.02	0.32

[a] By X-ray Fluorescence Spectrometer

[b] t-plot method

[c] less than 167.7 nm diameter at P/P_0=0.988

[d] $V_{meso}=V_{total}-V_{micro}$

Table S4 Acidic properties of different Pt-based bifunctional catalysts

Samples	Weak acid ($mmol\ g^{-1}$)[a]	Medium acid ($mmol\ g^{-1}$)[a]	Strong acid ($mmol\ g^{-1}$)[a]	Total acid ($mmol\ g^{-1}$)[a]	B/L[b]
Pt/ZSM-22	0.167	0.268	0.186	0.621	0.84
Pt-A/Z	0.137	0.153	0.145	0.435	0.32
Pt-Z/A	0.114	0.105	0.128	0.347	0.29
Pt/A+ZSM-22	0.106	0.131	0.128	0.365	0.51

[a] Acid amounts of catalysts were determined by NH_3-TPD results

[b] Ratios of Bronsted acid and Lewis acid were obtained from Pyridine-adsorbed FT-IR spectra

Table S5 Platinum and acid properties of bifunctional catalysts

Samples	Pt intake (wt%)[a]	Pt loading (wt%)[b]	Pt size (nm)[c]	D (%)[d]	n_{Pt} (μmol g^{-1})[e]	n_A (μmol g^{-1})[f]	n_{Pt}/n_A
Pt-A/Z	0.5	0.32	1.3	87	14.3	145	0.10
Pt-Z/A	0.5	0.23	1.7	66	7.4	128	0.06

[a] Metallic platinum content in $Pt(NH_3)_4(NO_3)_2$ or H_2PtCl_6 aqueous solutions used

[b] By inductively coupled plasma optical emission spectrometry

[c] The average Pt particle size was analyzed for the Pt-Z/A catalysts using over 200 particles in TEM images and for the Pt-A/Z catalyst using over 200 particles in HAADF-STEM images.

[d] Dispersion=$1.13/d_{Pt}$ size

[e] n_{Pt} denotes the density of surface Pt atoms, calculated by Pt ICP loadings and dispersion

[f] By deconvolution of NH_3-TPD profiles and integration of strong acid

Table S6 Properties of specification biofuel

Property		Details
Composition (wt.%)[a]		<C7:12.0
		C7-C20:27.0
		IP:48.8
		PC:8.4
		HP:3.8
Elemental Analysis (wt.%)[b]		C:81.05 H:18.14 O:0.71
Density (kg m^{-3})[c]	20 ℃	839
	40 ℃	824
Viscosity (mm^2 s^{-1})[d]	20 ℃	7.26
	40 ℃	4.29
Pour point (℃)[e]		-26.8
Flash point (℃)[f]		15.5
Heat of Combustion (MJ kg^{-1})[g]		46.4

[a] By Gas Chromatography.

[b] By CHONS Elemental Analyzer.

[c] ASTM D4052

[d] ASTM D445.

[e] ASTM D97.

[f] ASTM D93.

[g] ASTM D240.

Table S7 Binding energy for C 1s XPS of the catalysts

Peak number	Carbon specie	Catalyst							
		Ni/Al_2O_3		Spent Ni/Al_2O_3		Pt-A/Z		Spent Pt-A/Z	
		BE (eV)	Area(%)	BE (eV)	Area(%)	BE (eV)	Area(%)	BE (eV)	Area(%)
1	C-C/C-H	284.6	77.4	284.8	85.1	284.7	78.5	284.7	84.6
2	C-O	286.7	12.4	286.7	4.9	286.8	12.1	286.9	6.6
3	O-C=O	288.6	10.2	288.6	10	288.9	9.4	288.8	8.8

Table S8 Mass balance and carbon balance closures in different steady-state collection intervals under the optimal reaction conditions

TOS/h[a]	m_{feed}/g	m_{H2}/g[b]	C_{feed}/wt.%[c]	m_{org}/g	m_{aq}/g	m_{gas}/g	C_{org}/wt.%[c]	$m_{C,gas}$/g	Mass balance closure/%	Carbon balance closure/%
1-11-12	10.00	1.96	81.07	8.84	0.75	2.15	83.35	0.11	98.2	92.2
1-13-14	10.00	1.96	81.07	8.95	0.80	2.14	83.16	0.10	99.4	93.0
1-15-16	10.00	1.96	81.07	8.95	0.81	2.13	84.43	0.10	99.4	94.4
1-17-18	10.00	1.96	81.07	8.94	0.80	2.14	86.1	0.09	99.3	96.1
1-19-20	10.00	1.96	81.07	8.88	0.85	2.15	83.08	0.09	99.3	92.1
2-11-13	15.00	2.94	81.07	13.36	1.24	3.24	81.16	0.15	99.4	90.4
2-14-16	15.00	2.94	81.07	13.50	1.14	3.22	83.97	0.15	99.5	94.5
2-17-19	15.00	2.94	81.07	13.38	1.26	3.24	84.19	0.15	99.7	93.9

[a] The defined steady-state collection interval was 2 h and 3 h.

[b] The mass of H_2 was calculated from the measured hydrogen volume under 1 atm and 25 ℃, assuming ideal-gas behavior (V_m=24.465 L mol^{-1}).

[c] By CHONS elemental analyzer.

Supplementary Note 5 Discussion of mass and carbon balance closure

Although the carbon balance closure was slightly lower than the mass balance closure, it remained relatively high, demonstrating that most of the carbon in the feedstock was effectively accounted for in the organic liquid and gas products. The slightly lower carbon balance is primarily attributable to minor carbon fractions that may be associated with pathways that are difficult to quantify precisely, such as the continuous generation of a very small amount of deposited carbon during the steady-state interval, or the presence of trace oxygenated organic compounds in the aqueous phase. In this work, the contribution of these fractions was relatively small compared to that of the organic and gas phases and was therefore neglected in the calculations.

Table S9 Composition and amount of gaseous products collected under the optimal reaction conditions

TOS/h	V/L[a]	H_2/%	CO_2/%	C_2H_6/%	C_3H_8/%	iC_4H_{10}/%	nC_4H_{10}/%	iC_5H_{12}/%	nC_5H_{12}/%	m_{gas}/g[b]
1-11	12.24	99.669	0.014	0.061	0.153	0.023	0.047	0.006	0.005	1.076
1-12	12.24	99.694	0.012	0.059	0.150	0.023	0.050	0.006	0.006	1.076
1-13	12.24	99.602	0.012	0.057	0.147	0.023	0.050	0.006	0.006	1.075
1-14	12.24	99.741	0.014	0.051	0.126	0.019	0.040	0.005	0.005	1.065
1-15	12.24	99.726	0.015	0.053	0.134	0.021	0.042	0.004	0.005	1.068
1-16	12.24	99.738	0.014	0.054	0.129	0.019	0.038	0.004	0.004	1.065
1-17	12.24	99.744	0.012	0.049	0.126	0.020	0.040	0.005	0.004	1.064
1-18	12.36	97.956	0.014	0.048	0.124	0.019	0.039	0.004	0.004	1.075
1-19	12.36	98.181	0.017	0.048	0.128	0.020	0.040	0.004	0.004	1.077
1-20	12.36	99.746	0.022	0.044	0.121	0.019	0.039	0.004	0.004	1.074
2-11	12.24	99.707	0.011	0.073	0.134	0.019	0.045	0.006	0.005	1.082
2-12	12.24	99.727	0.009	0.066	0.126	0.018	0.044	0.006	0.006	1.078
2-13	12.24	99.714	0.009	0.068	0.131	0.018	0.046	0.007	0.006	1.080
2-14	12.24	99.718	0.010	0.069	0.130	0.017	0.043	0.007	0.005	1.069
2-15	12.24	98.348	0.010	0.067	0.125	0.016	0.040	0.006	0.005	1.077
2-16	12.24	99.738	0.012	0.068	0.124	0.016	0.037	0.004	0.004	1.075
2-17	12.24	98.003	0.010	0.065	0.126	0.016	0.040	0.006	0.004	1.077
2-18	12.36	97.713	0.008	0.066	0.131	0.017	0.044	0.006	0.004	1.078
2-19	12.36	99.719	0.008	0.069	0.141	0.019	0.048	0.007	0.004	1.083

[a] Measured using a wet gas meter

[b] The total gas mass was calculated from the measured gas volume at 1 atm and 25 °C using ideal-gas conversion (V_m=24.465 L mol^{-1}). As no N_2 was used in the experiment, the detected N_2 fraction was discarded, and the other components were normalized prior to calculation of the average molecular weight and gas mass.

Supplementary Note 6 Comparison of balance closure, productivity, and STY with industrial refence levels

For comparison, a 2024 report from the National Renewable Energy Laboratory (NREL) indicated that in industrial practice, the mass balance closure and carbon balance closure for renewable diesel production from vegetable oil via hydrodeoxygenation-hydroisomerization can reach 100% and 99%.[4] In comparison, the mass balance and carbon balance results obtained in this study are reasonably close to these industrial reference levels, suggesting that the present system already achieves good mass and carbon closure performance under continuous operation. In contrast, productivity and STY data for industrial units are rarely reported directly in the open literature. Based on a rough estimate using a typical industrial liquid hourly space velocity (LHSV) of about 1 h^{-1} and an organic hydrocarbon yield of

approximately 80%, the productivity and STY of the organic-phase products are on the order of 0.57 g g_{cat}^{-1} h^{-1} and 400 g L_{bed}^{-1} h^{-1}, respectively. Compared with this estimated industrial benchmark, the values obtained in the present work are relatively lower, but this difference can be reasonably understood and does not necessarily indicate poor process feasibility. First, the present study is still at the laboratory scale, where heat transfer, fluid distribution, and process integration have not yet reached the optimization level of industrial fixed-bed units. It is particularly noteworthy that, because of the small diameter of the fixed-bed reactor used in this work, the catalyst bed bulk density is only 0.375 kg·L^{-1}, which is about half of the typical bulk density of industrial fixed-bed catalysts (approximately 0.7 kg L^{-1}).[5] This lower bed bulk density directly reduces the amount of active catalyst accommodated per unit bed volume and therefore significantly lowers the STY calculated on a bed-volume basis. Second, the feedstock used here is CNSL, a biomass-derived raw material with a complex chemical composition, relatively high oxygen content, and strong reactivity. The reaction difficulty is clearly higher than that of the more conventional, relatively simple lipid-type feedstocks typically used in industrial hydrotreating. Consequently, achieving efficient conversion and a highly selective product distribution under the same scale and operating conditions is intrinsically more challenging. Third, the productivity and STY evaluation in this study is based on the production of SAF-range target products, rather than on maximizing the production of renewable diesel, which is more common in industrial practice. Compared with renewable diesel, obtaining SAF-range products generally requires more extensive hydroisomerization and moderate cracking, which means that the feedstock must maintain a longer effective contact time with the catalyst, inevitably reducing the productivity metrics on a time- and bed-volume basis. Therefore, the lower productivity and STY values obtained in this study relative to the estimated industrial benchmark should be understood as a consequence of the current laboratory-scale development stage, the bed packing characteristics, and the combined complexity of the feedstock and the process, rather than being simply interpreted as poor process feasibility. Overall, combined with the high mass balance and carbon balance closures, good reproducibility, and stable continuous operation, the system can be considered to have already established a solid foundation for further optimization and scale-up.

References

1 C. G. Piscopo, M. Schwarzer, M. Herrmann, A. Affini, P. Pelagatti, G. Maestri, R. Maggi and S. Loebbecke, *ChemCatChem*, 2016, **8**, 1293–1297.

2 I. Martinez-Botella, S. Littler, M. Kundra and C. H. Hornung, *Tetrahedron Green Chem*, 2023, **2**,100014.

3 J. Palo, M. Reinikainen, S. Rautiainen, A. T. Pasanen, D. Baudouin, H. Grénman and J. Lehtonen, *Applied Catalysis A: General*, 2025, **699**, 120172.

4 O. Rosales Calderon, L. Tao, Z. Abdullah, M. Talmadge, A. Milbrandt, S. Smolinski, K. Moriarty, A. Bhatt, Y. Zhang, V. Ravi, C. Skangos, R. Davis and C. Payne, *Sustainable Aviation Fuel State-of-Industry Report: Hydroprocessed Esters and Fatty Acids Pathway*, 2024.

5 G. C. Laredo, A. Montesinos and J. A. De Los Reyes, *Applied Catalysis A: General*, 2004, **265**, 171–183.